Electroblown titanium dioxide and titanium dioxide/silicon dioxide submicron fibers with and without titania nanorod layer for strontium(II) uptake

Paajanen, Johanna

2022-12-10

Paajanen , J , Pettilä , L O , Lönnrot , S , Heikkilä , M , Hatanpää , T , Ritala , M & Koivula , R 2022 , ' Electroblown titanium dioxide and titanium dioxide/silicon dioxide submicron fibers with and without titania nanorod layer for strontium(II) uptake ' , Chemical Engineering Journal Advances , vol. 13 , 100434 , pp. 1-12 . https://doi.org/10.1016/j.ceja.2022.100434

http://hdl.handle.net/10138/355849
https://doi.org/10.1016/j.ceja.2022.100434

Chemical Engineering Journal Advances 13 (2023) 100434

Contents lists available at ScienceDirect

Chemical Engineering Journal Advances

journal homepage: www.sciencedirect.com/journal/chemical-engineering-journal-advances

Electroblown titanium dioxide and titanium dioxide/silicon dioxide submicron fibers with and without titania nanorod layer for strontium (II) uptake

Johanna Paajanen *, Lauri Pettilä, Satu Lönnrot [1], Mikko Heikkilä, Timo Hatanpää, Mikko Ritala, Risto Koivula

Department of Chemistry, P.O. Box 55, FI-00014 University of Helsinki, Finland

ARTICLE INFO

Keywords:
Electroblowing
Titanium dioxide submicron fibers
Titania/silica composite fibers
Hydrothermal synthesis
Rutile titania nanorods
Strontium separation

ABSTRACT

Nuclear power is a clean alternative to fossil fuels. However, the use of nuclear energy generates hazardous fission products of which ^{90}Sr is the second most important. To remove Sr^{2+} from aqueous solutions, we synthesized submicron TiO_2 and TiO_2/SiO_2 composite fibers with Ti : Si molar ratios of 3 : 1 ($3TiO_2$–$1SiO_2$) and 1 : 1 ($1TiO_2$–$1SiO_2$) utilizing a novel electroblowing technique. After calcination at 500 °C, the TiO_2 and $3TiO_2$–$1SiO_2$ fibers had a predominantly anatase TiO_2 structure with portions of rutile and brookite but the crystallites in the $3TiO_2$–$1SiO_2$ fibers were smaller due to the SiO_2 component. The $1TiO_2$–$1SiO_2$ fibers were quasi-amorphous. Rutile TiO_2 nanorods were grown on the fibers by a hydrothermal method. The rods seemed to grow only on the TiO_2 domains of the fiber surface, which affected their size and morphology. In batch adsorption experiments all the fibers had excellent Sr^{2+} uptake with the hydrothermally modified TiO_2 fibers having the highest distribution coefficient (K_d) of 3,490,000 mL g^{-1}. The results show that both anatase and rutile TiO_2 can efficiently adsorb Sr^{2+} from an aqueous environment. Hardly any damage was observed in the nanorods on the TiO_2 fibers in a column operation test with flow rates up to 74 mL h^{-1} which is promising for the use of the fibers in industrial column mode wastewater treatment.

1. Introduction

To reduce greenhouse gas emissions and mitigate climate change, global energy is increasingly produced from clean low-carbon sources including nuclear power. However, in nuclear power plants, radioactive fission and activation products that are hazardous to human health and the environment are generated. Strontium-90 is the second most important fission product in nuclear power plant wastewaters [1]. Because of its relatively long half-life of 29 years, ^{90}Sr is highly radiotoxic for living organisms. In plants, it accumulates in the leaves and in animals, preferentially in the shells and fish scales [2]. Due to their chemical similarity, ^{90}Sr can replace calcium in the human bones causing cancers of the bone, bone marrow and soft tissues around the bone [3]. In order to protect human health and other living organisms, ^{90}Sr must be removed from nuclear waste effluents.

For separation of harmful metal ions from aqueous solutions, there are various techniques including chemical precipitation, membrane filtration, ion exchange, adsorption, electrochemical methods and phytoremediation [4,5]. Adsorption has some benefits over the other methods such as a good uptake efficiency even from dilute solutions, simple design, less toxic sludge formation and cost-effectiveness [4,6]. Adsorbents comprise both organic and inorganic materials that may be synthetic or of natural origin, such as agricultural by-products. Inorganic materials suit well for industrial wastewater treatment due to their high resistance to decomposition at elevated temperatures and upon exposure to ionizing radiation, and operation in a wide pH range. Additionally, inorganic adsorbents tend to have superior selectivity towards the target metal ions compared with organic materials.

Titanium dioxide is a nontoxic, chemically stable and fairly inexpensive material that has versatile applications. Nanoscale TiO_2 exhibits photocatalytic activity and is used for example for degradation of organic pollutants in wastewaters. Bare and modified anatase [7–14] and rutile [15,16] TiO_2 nano- and microparticles have also proved as efficient adsorbents for metal ions from water. However, when used in a

* Corresponding author.
E-mail address: johanna.paajanen@helsinki.fi (J. Paajanen).
[1] Present address: Kemira Oyj, P.O. Box 330, 00101 Helsinki, Finland.

https://doi.org/10.1016/j.ceja.2022.100434

Available online 10 December 2022

dynamic flow-through column, metal oxide particles have drawbacks such as poor mechanical stability, pressure build-up in the column and slow adsorption kinetics [17]. Utilization of small and fragile particles is also quite difficult in industrial scale column operation. These problems can be overcome by engineering the material into a fibrous form [17]. Metal oxide submicron and nanofibers could be optimal sorbents for purification of industrial wastewaters. Inorganic fibers have large surface area due to a high surface-to-volume ratio and porosity, and this gives rise to a good adsorption capacity. Mechanical strength of the fibers can be further enhanced by incorporating an amorphous component, such as silicon dioxide [18]. Moreover, inorganic submicron and nanofibers would be ecological and economical materials for the treatment of nuclear power plant wastewaters, as they would reduce the volume of solid radioactive waste that requires permanent repository.

Recently, there has been research on fibrous TiO_2 for heavy metal separation from aqueous solutions. Nevertheless, in the published reports, TiO_2 is present only as a minor component in a polymeric matrix [19–21] and reports on bare TiO_2 fibrous sorbents are lacking. Bare metal dioxide and composite metal dioxide/silicon dioxide submicron fibers have efficiently and selectively adsorbed Sb^{5+} and Co^{2+} from aqueous solutions [17,18,22]. The efficient and selective adsorption is based on both the crystalline structure and large surface area of the fibers. The surface area, in turn, is affected by both the crystallite size and morphology of the fibers. The adsorption performance of metal oxide fibers can be optimized by combining the desired crystalline structure with a morphology customized to maximize the surface area. One approach to customize the morphology and increase the surface area of inorganic fibers is to prepare hierarchical structures, that is, to grow secondary structures on the primary fibers. For instance, TiO_2 [23] and V_2O_5 [24] nanorods were grown on TiO_2 fibers resulting in increased surface area and improvement in the antibacterial [23] and photocatalytic [24] activity. Commonly, the primary fibers have been prepared by electrospinning and the secondary nanostructures on them by hydro- or solvothermal methods.

Electrospinning is a conventional technique to prepare inorganic nano- and microfibers. In a typical electrospinning procedure, a high voltage is applied to a solution comprising a polymer, one or more solvents and a metal precursor. During the electrospinning process, the polymeric chains stretch due to repulsive electrostatic forces and deposit as fibers on a grounded collector. Through post-electrospinning calcination, the polymer is removed and the fibrous inorganic end product, typically metal oxide, is formed. Different solution compositions and process parameters allow to control the properties and morphology of the fibers [25]. Hence, electrospinning is a straightforward and cost-efficient technique and upscalable for industry [26–30]. By contrast, solution blowing method utilizes pressurized air to draw fibers from the precursor solution [31]. Solution blowing is even 15 times more productive than electrospinning [32] but it usually yields bundles of aligned fibers whereas electrospinning generates an entanglement of individual, un-aligned fibers [33,34]. In electroblowing, the fibers are formed by both electrostatic force and air flow and hence the method combines electrospinning and solution blowing and their merits. As compared with electrospinning, the assisting air flow in electroblowing makes it possible to use more viscous precursor solutions [35] and yields fibers with smaller diameters and fewer beads [36]. Furthermore, electroblowing enables 2.5 times faster fiber production than solution blowing [18,32]. Electroblowing should be as feasible to scale up for industry as electrospinning.

Here, we report on synthesis of TiO_2 and composite TiO_2/SiO_2 submicron fibers by electroblowing and calcination. We also report on synthesis of TiO_2 nanorods on the fibers by a hydrothermal method and how the amount of SiO_2 in the fibers as well as reaction time affect the synthesis products. Furthermore, we report on $^{85}Sr^{2+}$ uptake by the plain and hydrothermally modified fibers. To the authors' knowledge, this is the first report on electroblowing synthesis of TiO_2 and TiO_2/SiO_2 submicron fibers and on synthesis of TiO_2 nanorods on composite TiO_2/SiO_2 fibers. Moreover, this is the first report on Sr^{2+} uptake by the plain and hydrothermally modified TiO_2 and TiO_2/SiO_2 fibers.

2. Experimental

2.1. Materials

The precursor solutions for the electroblowing and the hydrothermal synthesis were prepared from titanium isopropoxide (TTIP, $Ti\{OCH(CH_3)_2\}_4$, 97%, Sigma-Aldrich), titanium butoxide ($Ti(OBu)_4$, $Ti\{O(CH_2)_3CH_3\}_4$, 97%, Sigma-Aldrich), tetraethoxysilane (TEOS, $Si(OCH_2CH_3)_4$, 98%, Sigma-Aldrich), ammonium acetate (NH_4OAc, $NH_4CH_3CO_2$, ≥98%, Merck), polyvinylpyrrolidone (PVP, $(C_6H_9NO)_n$, $M_W = 1{,}300{,}000$, Alfa Aesar), ethanol (EtOH, CH_3CH_2OH, 96 vol%, GPR RECTAPUR), glacial acetic acid (HOAc, CH_3COOH, Fisher Scientific) and hydrochloric acid (HCl, ≥37%, Sigma-Aldrich). In the Sr^{2+} uptake experiments, $^{85}SrCl_2$, $NaNO_3$ (≥99%, VWR Chemicals), HNO_3 (70%, Fisher Scientific), NaOH (1 M, Reagent Ph.Eur., VWR Chemicals), $Ca(OH)_2$, $Ca(NO_3)_2{\bullet}4H_2O$ (≥99%, Riedel-de Haën), $Mg(OH)_2$ (67–70%, May & Baker), $Mg(NO_3)_2{\bullet}6H_2O$ (≥99%, Merck), $Ba(OH)_2$ (technical grade, ~95%, Sigma-Aldrich), $Ba(NO_3)_2$ (≥99%, Sigma-Aldrich), $Sr(NO_3)_2$ (≥98%, Riedel-de Haën) and deionized water were used.

2.2. Synthesis of TiO_2 and TiO_2/SiO_2 fibers and hydrothermal modification

TiO_2 and composite TiO_2/SiO_2 fibers with different molar ratios of Ti and Si were prepared by electroblowing the respective precursor solutions followed by calcination of the as-electroblown fibrous mats. The precursor solution for the synthesis of TiO_2 fibers comprised 10 wt% TTIP, 2 wt% NH_4OAc, 7 wt% PVP, 58 wt% EtOH and 23 wt% HOAc. The precursor solution for the synthesis of composite fibers with a Ti : Si molar ratio of 3 : 1 (denoted as $3TiO_2$–$1SiO_2$) was comprised of 8 wt% TTIP, 2 wt% TEOS, 2 wt% NH_4OAc, 7 wt% PVP, 58 wt% EtOH and 23 wt % HOAc. The precursor solution for the synthesis of composite fibers with a Ti : Si molar ratio of 1 : 1 (denoted as $1TiO_2$–$1SiO_2$) comprised 5 wt% TTIP, 4 wt% TEOS, 1 wt% NH_4OAc, 7 wt% PVP, 59 wt% EtOH and 24 wt% HOAc. The solutions were stirred at room temperature until they were clear and homogeneous.

A self-made apparatus was used for the electroblowing [37]. In a typical procedure, 12 mL of the precursor solution was withdrawn into a syringe and a 27 G (ø 0.21 mm) needle was attached to the syringe tip. The syringe was placed on a syringe pump (KD Scientific Legato® 101) and the solution feed rate was adjusted to 15 mL h^{-1}. The feed rate was 4 to 375 times as high as reported for electrospinning of TiO_2 [38–45] and TiO_2/SiO_2 [45,46] fibers and 1.5 to 3 times as high as reported for solution blowing of TiO_2 fibers [47]. The needle was pushed through a 3 mm metallic nozzle mounted on a polycarbonate box enclosing a cylindrical side collector and a planar back collector at 80 cm distance, both made of metal wire mesh. A high voltage power source was used to set the potential difference between the needle and the grounded collectors to 15 kV. Compressed air was delivered through the nozzle at a rate of 30 NL min^{-1} and additional air was delivered to the box from the sides at a rate of 40 NL min^{-1} to enhance solvent evaporation and to keep the relative humidity within the box below 20%. The solution jet erupting from the needle deposited as fibers on the collectors. At the end of the experiment, the fibrous mats were detached and calcined in air at 500 °C for 2 (TiO_2 fibers) or 4 (TiO_2/SiO_2 fibers) hours with a heating rate of 1 °C min^{-1} in order to remove the polymer and to form the desired ceramic fibers. The yields of TiO_2 and TiO_2/SiO_2 fibers with Ti : Si molar ratios of 3 : 1 and 1 : 1 were at best 0.41, 0.30 and 0.33 g per hour of electroblowing, respectively.

For the hydrothermal synthesis, a solution containing 3 wt% Ti $(OBu)_4$, 20 wt% HCl and 77 wt% H_2O was prepared. A piece (0.02–0.1 g) of the calcined fibrous mat was placed in a 50 mL PTFE vessel and 20 mL of the solution was added into the vessel. The vessel was placed in a

stainless steel autoclave and the autoclave was put in an oven set to 150 °C. The duration of the hydrothermal reaction was varied from 1 to 5 h. The synthesis product was filtered using a Büchner funnel and washed with H_2O and a small amount of EtOH until the filtrate was neutral. The product was dried in an oven at 50 °C overnight.

2.3. Characterization of the TiO_2 and TiO_2/SiO_2 fibers

Fiber morphology was characterized by imaging with secondary electrons (SE) and transmitted electrons (TE) using a Hitachi S-4800 field emission scanning electron microscope (FESEM). Prior to the imaging with the secondary electrons, the samples were placed on carbon tape and sputter coated with a 4 nm layer of Au/Pd alloy to enhance conductivity. For the imaging with the transmitted electrons, the samples were placed on a folding support grid made of copper. Elemental analysis of the fibers was performed by an Oxford INCA 350 energy dispersive X-ray spectroscopy (EDX) system connected to the Hitachi S-4800. The average diameters of the fibers as well as the average diameters and lengths of the TiO_2 nanorods were determined with a Fiji ImageJ software. The crystallinity of the fibers was characterized by a PANalytical X'Pert PRO MPD X-ray diffractometer using Cu Kα radiation and focusing optics. The fibrous samples were powdered prior to the characterization. The mean crystallite sizes were determined from the XRD data by the Rietveld refinement using a MAUD software [48]. Thermogravimetric analysis (TGA) of the as-electroblown fibers was conducted using a Mettler-Toledo TGA/DSC 3+ thermal analysis system. A heating rate of 10 °C min^{-1} in a temperature range of 25 to 1000 °C was used in a flow of air (50 mol%) and N_2 (50 mol%, the purge gas). The specific surface area and porosity of the fibers were measured by N_2 physisorption at 77 K using a Micromeritics ASAP 2020 surface area and porosity analyser.

2.4. Sr^{2+} uptake studies

2.4.1. Effect of SiO_2 content and hydrothermal modification

Sr^{2+} uptake by the TiO_2 and TiO_2/SiO_2 fibers with and without a hydrothermal modification was studied at a pH of 11.5. 20 mg of fibers were weighed into 20 mL scintillation vials and 10 mL of 0.1 M $NaNO_3$ solution containing 100 Bq mL^{-1} $^{85}Sr^{2+}$ ($1.34{\cdot}10^{-12}$ M) was added into the vials. NaOH was used to adjust the solution pH to 11.5. The samples were equilibrated in a constant rotary mixer (50 rpm) for one day after which the equilibrium pH was measured. The samples were phase separated by centrifugation at 4000 rpm (2100 g) and syringe filtration (Acrodisc LC PVDF, 0.2 μm). The $^{85}Sr^{2+}$ uptake of each sample was determined by taking a 5 mL aliquot of the filtrate and measuring the remaining activity with a PerkinElmer Wallac Wizard 3″ 1480 automatic gamma counter. The $^{85}Sr^{2+}$ uptake results are presented by means of distribution coefficient K_d, that describes the distribution of the adsorbate between the adsorbent and solution:

$$K_d = \frac{(c_0 - c_{eq})V}{c_{eq}m} \quad (1)$$

where c_0 (Bq L^{-1} or M) is the initial concentration, c_{eq} (Bq L^{-1} or M) is the equilibrium concentration, V (mL) is the volume of the solution and m (g) is the mass of dry adsorbent. Background activity was subtracted before the calculations. Uncertainty of K_d was calculated using the error propagation law.

2.4.2. Effect of pH

$^{85}Sr^{2+}$ uptake by the TiO_2 fibers was studied over a pH range of 4 to 12. 20 mg of fibers were weighed into 20 mL scintillation vials and 10 mL of 0.01 M $NaNO_3$ solution containing 30 Bq mL^{-1} $^{85}Sr^{2+}$ ($4.03{\cdot}10^{-13}$ M) was added into the vials. The pH of each sample was approximately adjusted with HNO_3 or NaOH and the samples were equilibrated for 1 h after which the pH of each sample was accurately adjusted. The samples were equilibrated for 24 h and phase separated, and the remaining activity was measured as described above. The equilibrium pH was determined from the remaining sample.

2.4.3. Zeta potential

Zeta potential as a function of pH was determined for the TiO_2 fibers after the adsorption of $^{85}Sr^{2+}$. 0.8 mL aliquots were taken from the samples used in the pH effect experiment after the equilibration of 24 h but before the phase separation. Zeta potential of the samples was measured using Malvern Zetasizer Nano ZC.

2.4.4. Effect of coexisting ions

Effect of coexisting ions Na^+, Mg^{2+}, Ca^{2+} and Ba^{2+} on the $^{85}Sr^{2+}$ uptake by the TiO_2 fibers was examined at pH of 9. Concentrations of 0.001, 0.01, 0.1 and 1 M were used for Na^+ and concentration of 0.01 M for Mg^{2+}, Ca^{2+} and Ba^{2+}. $^{85}Sr^{2+}$ concentration was 30 Bq mL^{-1} ($4.03{\cdot}10^{-13}$ M). For the experiments on Na^+, 40 mg of fibers were weighed into 20 mL scintillation vials and 10 mL of $NaNO_3$ was added into the vials. The pH of the samples was adjusted to 9 with NaOH. The samples were equilibrated and phase separated and the remaining activity was measured as described before. For the experiments on Mg^{2+}, Ca^{2+} and Ba^{2+}, 20 mg of fibers were weighed into 20 mL scintillation vials and 10 mL 0.01 M $Mg(OH)_2$, $Mg(NO_3)_2$, $Ca(OH)_2$ or $Ba(OH)_2$ was added into the vials. The final pH adjustment was done with the corresponding metal hydroxide solution and also NaOH for the Ca^{2+} samples and one of the Ba^{2+} samples. The samples were equilibrated and measured as described earlier.

2.4.5. EDX analysis

Elemental analysis before and after adsorption of Sr^{2+} was conducted by EDX for the plain and hydrothermally modified TiO_2 fibers and plain TiO_2/SiO_2 fibers. 20 mg of fibers were weighed into 20 mL scintillation vials and 10 mL of 0.02 M non-radioactive $Sr(NO_3)_2$ was added into the vials. The pH of the solution was adjusted to 11.5 using NaOH. The samples were equilibrated for five days, phase separated, washed with deionized water and dried in an oven at 70 °C overnight.

2.4.6. Durability in column operation

Durability of the hydrothermally modified TiO_2 fibers (3 h reaction) was tested in column operation. 200 mg of fibers were mixed with 0.01 M $NaNO_3$ and packed into a ø 1 cm column. After this, 0.01 M $NaNO_3$ was fed through the column with increasing rates of 4.6, 9.2, 18.6, 36.9 and 73.5 mL h^{-1} with a time of one hour for each rate.

3. Results and discussion

3.1. Thermogravimetric analysis of the TiO_2 and TiO_2/SiO_2 fibers

Fig. 1 shows photographs of as-electroblown TiO_2/PVP and TiO_2/SiO_2/PVP fibers as well as TiO_2 and TiO_2/SiO_2 fibers after calcination at 500 °C. The calcined fiber mats have shrunk because the polymer has been removed. The white color of the calcined fibers implies that there are no significant amounts of carbonaceous residues so the combustion of the polymer has been quite complete.

As can be seen from the TG curves (Fig. 2), the mass decrease of the as-electroblown fibers is the most intense at 300–500 °C which is due to the release and combustion of pyrrolidone substituents and decomposition and combustion of polyenic sequences of PVP [49]. In the mixed air/N_2 atmosphere used in the TG analysis, the mass decrease is completely over at 600, 650 and 700 °C for TiO_2, $3TiO_2$–$1SiO_2$ and $1TiO_2$–$1SiO_2$ fibers, respectively (Fig. 2). The amorphous SiO_2 component in the composite fibers might be more prone to retain the amorphous polymer compared with the crystalline TiO_2 fibers and thereby could retard its combustion, which is supported by our previous results [18].

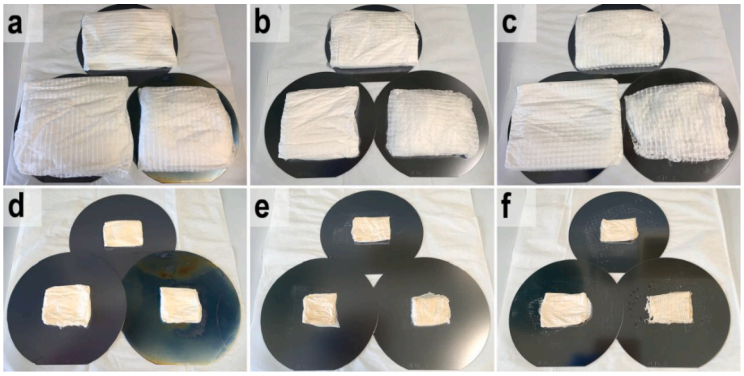

Fig. 1. As-electroblown TiO_2/PVP (a), $3TiO_2$–$1SiO_2$/PVP (b) and $1TiO_2$–$1SiO_2$/PVP (c) fibers as well as TiO_2 (d), $3TiO_2$–$1SiO_2$ (e) and $1TiO_2$–$1SiO_2$ (f) fibers calcined at 500 °C on 150 mm silicon wafers. The calcined fiber mats have shrunk as the polymer has been removed.

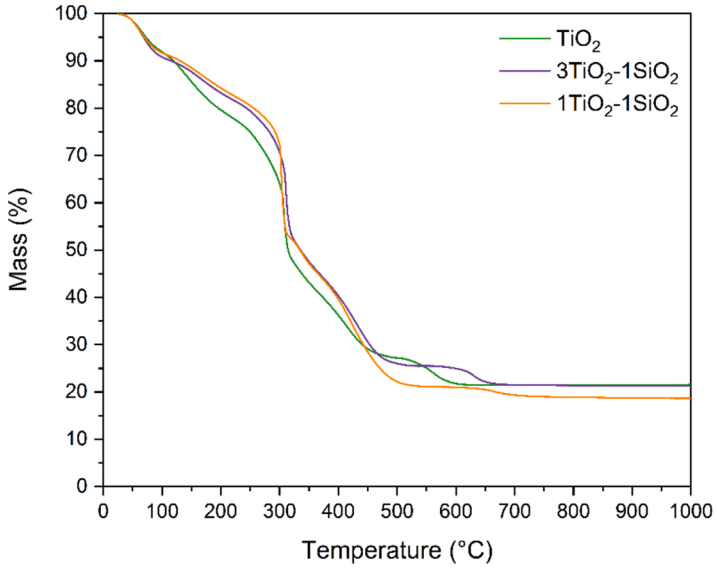

Fig. 2. Thermogravimetric curves of as-electroblown TiO_2/PVP and TiO_2/SiO_2/PVP fibers in air (50 mol%) and N_2 (50 mol%, the purge gas).

Fig. 2 also shows that the residual mass, i.e. the mass of the bare ceramic fibers, is ca. 20% for TiO_2 and $3TiO_2$–$1SiO_2$ fibers while it is ca. 17% for $1TiO_2$–$1SiO_2$ fibers. This is in accordance with the measured weights of the as-electroblown and calcined fibers and indicates pure synthesis products. The color of the calcined fibers and TG results confirm that the calcination temperature of 500 °C and calcination time of 2 h for the TiO_2 and 4 h for the $3TiO_2$–$1SiO_2$ and $1TiO_2$–$1SiO_2$ fibers in the air atmosphere should be sufficient to remove the PVP and form the desired ceramic materials. Both the bare TiO_2 and composite TiO_2/SiO_2 fiber mats were robust and elastic and could be bent without breaking.

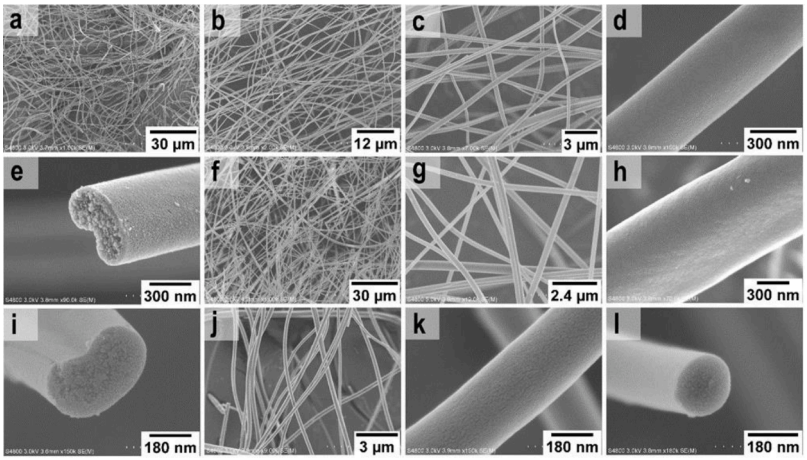

Fig. 3. FESEM images of as-electroblown TiO_2/PVP (a) and $3TiO_2$–$1SiO_2$/PVP (f) fibers and TiO_2 (b–e), $3TiO_2$–$1SiO_2$ (g–i) and $1TiO_2$–$1SiO_2$ (j–l) fibers calcined at 500 °C.

The robustness and elasticity of the fibers are demonstrated in the video "Bending experiments with the TiO_2 and TiO_2/SiO_2 fibers".

3.2. Electron microscopy and EDX analysis of the TiO_2 and TiO_2/SiO_2 fibers

FESEM images of the as-electroblown TiO_2/PVP and $3TiO_2$–$1SiO_2$/PVP fibers as well as the calcined TiO_2, $3TiO_2$–$1SiO_2$ and $1TiO_2$–$1SiO_2$ fibers are presented in Fig. 3. The calcined fibers appeared smooth and had a dense structure, as revealed by TEM images (Fig. 4). The as-electroblown TiO_2/PVP and $3TiO_2$–$1SiO_2$/PVP fibers had some conjoined fibers probably owing to incomplete solvent evaporation and the fibers remained conjoined after calcination. Huang et al. also observed that as-electrospun TiO_2 and TiO_2/SiO_2 fibers with a TiO_2 content of 75 and 90 mol% were ribbon-shaped with a dumbbell-shaped cross-section [45]. The average diameter of the as-electroblown fibers containing PVP was ca. 1 μm and the average diameters of the calcined fibers were 440, 380 and 290 nm for TiO_2, $3TiO_2$–$1SiO_2$ and $1TiO_2$–$1SiO_2$ fibers, respectively.

Photographs of TiO_2 and $1TiO_2$–$1SiO_2$ fibers after a 3 h hydrothermal synthesis of TiO_2 nanorod layer are shown in Fig. S1. Fig. 5a–g show FESEM images of hydrothermally modified (3 h reaction) TiO_2, $3TiO_2$–$1SiO_2$ and $1TiO_2$–$1SiO_2$ fibers. FESEM images of TiO_2 fibers after hydrothermal modifications of 1, 2, 4 and 5 h are shown in Fig. 5h–l. The morphologies of the TiO_2 and $3TiO_2$–$1SiO_2$ fibers after the 3 h hydrothermal modification resemble each other whereas the $1TiO_21SiO_2$ fibers have a different morphology. On the TiO_2 and $3TiO_2$–$1SiO_2$ fibers, the TiO_2 nanorods were tetragonal or tapered and quite uniform in size forming a compact layer. Nanostructured TiO_2 that has been synthesized on a rutile or anatase substrate in acidic hydrothermal conditions typically adopts a tetragonal or tapered rod-like morphology [50–55]. On the $1TiO_2$–$1SiO_2$ fibers, the TiO_2 nanorods were more sparse and mainly tapered and some of the rods were star-shaped or branched with smaller rods protruding from them. TiO_2 was also deposited as small 30–100 nm grains on the $1TiO_2$–$1SiO_2$ fibers. The average lengths of the TiO_2 nanorods were 430, 850 and 1130 nm and the average diameters were 70, 100 and 200 nm for the TiO_2, $3TiO_2$–$1SiO_2$ and $1TiO_2$–$1SiO_2$ fibers, respectively. The TiO_2 nanorods grew the larger the more SiO_2 the fibers contained (Fig 5d–g and Fig. 7). The results imply that in the $3TiO_2$–$1SiO_2$ and especially $1TiO_2$–$1SiO_2$ fibers, the SiO_2 component limits the nucleation and growth of TiO_2 nanorods on the pristine fiber surface and instead, TiO_2 is deposited on the existing nanorods as the hydrothermal reaction proceeds. On the $3TiO_2$–$1SiO_2$ fibers, the deposition of TiO_2 on the nanorods seems to result in a growth of the length and diameter of the rods. On the $1TiO_2$–$1SiO_2$ fibers, the deposition of TiO_2 on the nanorods appears to result in both growth of the rods and formation of the star-shaped and branched rod structures. The results suggest that TiO_2 nanostructures grow on the TiO_2 domains but not on the SiO_2 domains of the fiber surface. Further evidence for this was provided by hydrothermal syntheses on bare SiO_2 fibers, after which no growth of TiO_2 nanostructures on the fibers was observed (Fig. S2). Similarly to the fiber substrates, the TiO_2 nanorods had a dense character as confirmed by TEM analysis (Fig. 6).

The duration of the hydrothermal synthesis affected the amount, length and diameter of the TiO_2 nanorods deposited on the TiO_2 fibers (Fig. 5h–l). A reaction time of 1 h produced scattered TiO_2 nanorods that were ca. 100 nm long and 30 nm in diameter while a reaction time of 5 h resulted in a compact layer of TiO_2 nanorods that were ca. 600 nm long and 100 nm in diameter. The dependence of the TiO_2 nanorod size on the hydrothermal reaction time is illustrated in Fig. 8. We also performed a hydrothermal synthesis of 3 h twice for the same fibers. After the second synthesis, the TiO_2 nanorods had grown on average 70% in length and 10% in diameter. After two syntheses, the nanorod layer on the fibers also appeared thicker than after one synthesis (Fig. S3). The results suggest that during the second hydrothermal reaction, TiO_2 is mostly grown on top of the existing TiO_2 nanorods but new nanorods possibly also grow on available fiber surface. The fibers endured two hydrothermal reactions well, since hardly any damage such as fractures was observed in the fiber substrates or the nanorods after the second reaction (Fig. S3d–f).

EDX spectra and semiquantitative elemental analysis results of the plain and hydrothermally modified TiO_2 fibers and the plain $3TiO_2$–$1SiO_2$ and $1TiO_2$–$1SiO_2$ fibers are shown in Fig. S4–S7. Due to possible variation in sample homogeneity and difficult quantification of light elements by EDX, and because the detected carbon may also originate from the environment, the quantified molar percentages of silicon and oxygen as well as residual carbon cannot be considered reliable. However, the relative amount of detected silicon is higher in the $1TiO_2$–$1SiO_2$ than $3TiO_2$–$1SiO_2$ fibers, as expected.

3.3. Crystal structure analysis of the TiO_2 and TiO_2/SiO_2 fibers

X-ray diffractograms of the plain TiO_2, $3TiO_2$–$1SiO_2$ and $1TiO_2$–$1SiO_2$ fibers and of the fibers after a hydrothermal modification of 3 h are presented in Fig. 9. The determined crystalline phases and crystallite sizes and the weight ratio of each phase are presented in Table 1. The crystallinity of the plain fibers increased along with their TiO_2 content. The $1TiO_2$–$1SiO_2$ fibers were quasi-amorphous lacking any long-range crystalline order and no crystalline phase or crystallite size could be determined for them. The $3TiO_2$–$1SiO_2$ fibers were moderately crystalline and the TiO_2 fibers were highly crystalline. Anatase was the predominant phase in the plain TiO_2 and $3TiO_2$–$1SiO_2$ fibers. This is in accordance with results on electrospun TiO_2 submicron and nanofibers calcined at 450–600 °C [38–45] and electrospun TiO_2/SiO_2 submicron and microfibers with a TiO_2 content of 50–90 mol % calcined at 1000 °C [45], with a TiO_2 content of 64 mol% calcined at 600 °C [46] and with a TiO_2 content of 72–89 mol% calcined at 700 °C [56]. In this study, in the plain TiO_2 fibers 13 wt% rutile and 11 wt%

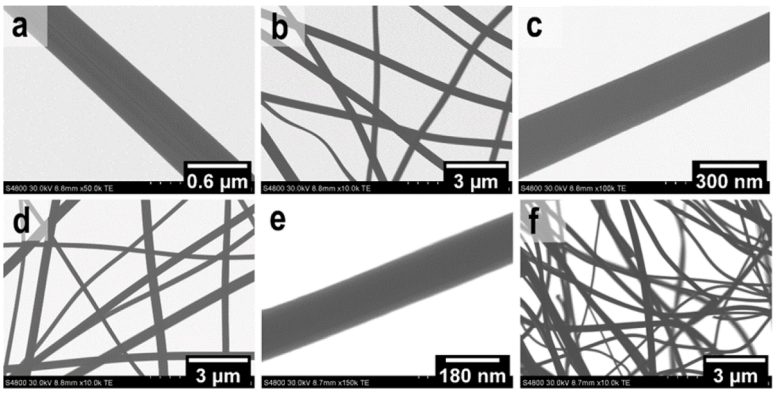

Fig. 4. TEM images of TiO_2 (a and b), $3TiO_2$–$1SiO_2$ (c and d) and $1TiO_2$–$1SiO_2$ (e and f) fibers.

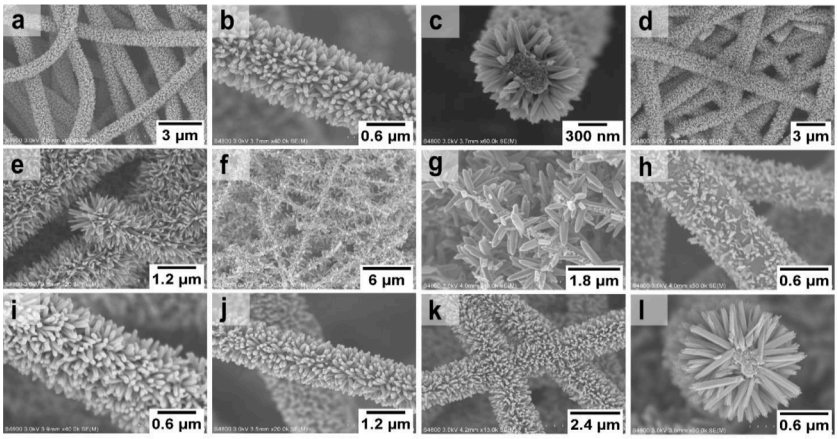

Fig. 5. FESEM images of TiO_2 (a–c), $3TiO_2$–$1SiO_2$ (d and e) and $1TiO_2$–$1SiO_2$ (f and g) fibers after a hydrothermal synthesis of 3 h as well as TiO_2 fibers after 1 (h), 2 (i), 4 (j) and 5 (k and l) hours of hydrothermal synthesis.

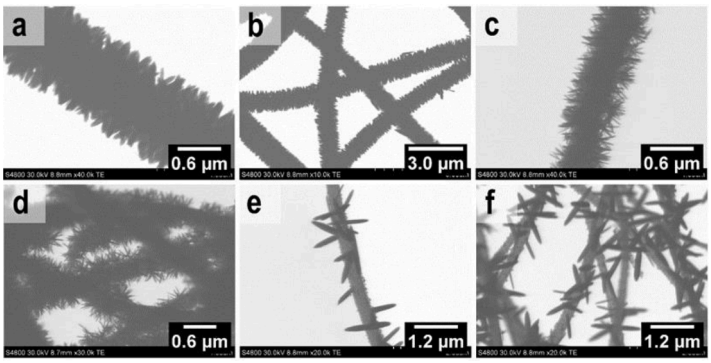

Fig. 6. TEM images of hydrothermally modified (3 h) TiO_2 (a and b), $3TiO_2$–$1SiO_2$ (c and d) and $1TiO_2$–$1SiO_2$ (e and f) fibers.

Table 1
Crystalline phases, respective weight ratios and average crystallite sizes of plain and hydrothermally modified (ht TiO_2, 3 h reaction) TiO_2 and TiO_2/SiO_2 fibers. A, B, R, is. and anis. denote anatase, brookite, rutile, isotropic and anisotropic, respectively.

	Av. cryst. size (nm)					Phase ratio (wt %)		
Fibers	A is.	A anis.[a]	R is.	R anis.[a]	B is.	A	R	B
$3TiO_2$–$1SiO_2$[b]	7–9		7–9		7–9	53	10	37
TiO_2	21	22 [100] 12 [001]	16		12	76	13	11
$1TiO_2$–$1SiO_2$ + ht TiO_2			20	13 [100] 37 [001]	25		97	3
$3TiO_2$–$1SiO_2$ + ht TiO_2	9		23	16 [100] 51 [001]		8	92	
TiO_2 + ht TiO_2	21		18	13 [100] 38 [001]		17	83	

a: If anis. value is provided, a better fit was achieved with the anisotropic crystallite size modeling. In those cases is. value is an average. *b*: Brookite is definitely present due to the bump at 30° 2θ and the fibers seem to be a mixture of anatase and brookite with possibly a small fraction of rutile included. Exact phase composition is difficult to determine and a large error is possible in the results. The crystallite sizes seem to be between 7 and 9 nm.

brookite were also detected. This mixed anatase/rutile/brookite composition of TiO_2 fibers calcined at 500 °C is rather unique, since previously only traces of either brookite [40] or rutile [44] have been observed in anatase TiO_2 fibers calcined at 500–550 °C. However, such a three-phase mixture has been reported for TiO_2 powder calcined at 500 °C [57]. In the $3TiO_2$–$1SiO_2$ fibers 37 wt% brookite and 10 wt% rutile were also present besides anatase. All the TiO_2 phases had *d* values matching with literature references which proves that SiO_2 had not mixed with TiO_2. Thus the fibers are a four-constituent composite of anatase, brookite and rutile TiO_2 and amorphous SiO_2.

As regards the TiO_2 fibers, the best fit to the measured XRD data was achieved with an anisotropic anatase crystallite size of 22 and 12 nm for the longest and shortest dimension, respectively. An anisotropic anatase crystallite size of 46 and 23 nm was also reported for TiO_2 powder calcined at 500 °C [57]. The rutile and brookite crystallite sizes were isotropic and on average 16 and 12 nm, respectively. In the $3TiO_2$–$1SiO_2$ fibers the crystallite sizes of all the three phases were isotropic but smaller, 7–9 nm. The SiO_2 component presumably hinders the TiO_2 crystallite growth, in a similar way to SnO_2/SiO_2 composite fibers with the same Sn : Si molar ratio of 3 : 1 [18]. A mixture of anatase TiO_2 and amorphous SiO_2 nanograins was observed in TiO_2/SiO_2 microfibers with a Ti : Si molar ratio of 89 : 11 calcined at 700 °C [56]. The $1TiO_2$–$1SiO_2$ fibers are probably also a mixture of nanogranular anatase and brookite TiO_2 and amorphous SiO_2 but with a larger amount of SiO_2.

As for the hydrothermally modified fibers, the diffraction patterns were mainly of the rutile phase. In the hydrothermally modified TiO_2 and $3TiO_2$–$1SiO_2$ fibers some anatase was also present owing to the anatase fiber substrate. In the hydrothermally modified $1TiO_2$–$1SiO_2$ fibers 3 wt% brookite was detected. This could be due to the small grains on the fibers that may have the brookite structure (Fig. 5f and g). The rutile peaks are clearly due to the hydrothermally grown TiO_2 nanorods. It is known that TiO_2 nanorods grown in acidic hydrothermal solution on an anatase [51,52] or rutile [50,53–55] substrate have the rutile structure. The rutile crystal sizes were anisotropic being 13–16 nm in the [100] direction and 37–51 nm in the [001] direction. Considering the average diameter of 70–200 nm and length of 430–1130 nm of the TiO_2

nanorods after 3 h hydrothermal synthesis (Fig. 7), the rods were polycrystalline. The results indicate that the crystals grow preferentially in the [001] direction, which is supported by previous studies [52,55]. In nanoscale rutile TiO_2, the (001) face grows faster than the other faces because of the highest number of corners and edges available for sharing in the TiO_6 octahedra [55]. On this basis, in the present study, the crystals in the nanorods are most likely aligned parallel to the longitudinal axis of the rods, as the square cross-section of the rods also implies. Closer inspection of individual nanorods reveals that the rods are composed of pillars of ca. 10–20 nm in diameter, which coincides with the approximated shorter crystal dimensions of 13–16 nm (Fig. S16, Table 1). The pillars are probably the crystals of the nanorods.

3.4. Specific surface area, pore volume and pore size analysis of the TiO_2 fibers

To study the effect of the hydrothermally grown TiO_2 nanorods on the surface area of the fibers and the porosity of both the plain and hydrothermally modified fibers, specific surface area, pore volume and pore size analysis was conducted on TiO_2 fibers without and with a hydrothermal modification of 3 h. The specific surface area was determined by the Brunauer-Emmett-Teller (BET) method and the total pore volume, pore size distribution and average pore diameter by the Barrett-Joyner-Halenda (BJH) method using nitrogen gas adsorption and desorption. As shown in Table 2, the specific surface area and pore volume of the fibers are 5 and 7 times higher after the hydrothermal modification, respectively. The fibers are mesoporous with 6 and 8 nm pores for the plain and hydrothermally modified fibers, respectively. The specific surface area of the plain fibers is somewhat lower than the values 49–61.5 $m^2\ g^{-1}$ reported previously for TiO_2 submicron fibers calcined at 500 [40] and 550 °C [41]. This is apparently caused by the larger average diameter of the fibers in this study. N_2 adsorption and desorption isotherms as well as pore size distribution for the plain and hydrothermally modified TiO_2 fibers are presented in Fig. S12–S15.

3.5. Sr^{2+} uptake by the TiO_2 and TiO_2/SiO_2 fibers

3.5.1. Effect of pH on Sr^{2+} uptake and surface charge of the fibers

The effect of solution pH on the Sr^{2+} uptake by the TiO_2 fibers and on surface charge of the fibers was investigated. Up to pH of ca. 6 the sorption of Sr^{2+} and K_d values are fairly low but begin to increase rapidly above this point (Fig. 10). The sorption of Sr^{2+} almost reaches a maximum at pH of 10 but the K_d values still increase up to pH 12. The pH of ca. 6 above which the Sr^{2+} uptake markedly improves coincides with the isoelectric point (IEP) of 6.1 of the fibers (Fig. 11). The adsorbed Sr^{2+} is likely to have a negligible effect on the IEP and zeta potential of the TiO_2 fibers, because the concentration of Sr^{2+} is so low and the uptake is very weak below the IEP. The measured IEP 6.1 is close to the literature values of 5.4–6.7 for anatase [7,9,10,13,14] and 5.4 for rutile [16] TiO_2 particles. Moreover, similar enhancement in Sr^{2+} uptake in the basic pH region above the IEP has been observed previously with anatase [7,9,13,14] and rutile [16] TiO_2 particles. As can be seen from Fig. 11, the surface of the fibers is negatively charged above the IEP which is explained by growing number of Ti-O^- groups due to deprotonation of surface Ti-OH groups [13,14]. The enhanced Sr^{2+} uptake at pH values higher than the IEP suggests that the uptake is initiated by electrostatic attraction between the negatively charged Ti-O^- groups and Sr^{2+}, which is the prevalent Sr species up to pH of 13 [13,14,58].

3.5.2. Sr^{2+} uptake by the plain and hydrothermally modified fibers

The distribution coefficients K_d for Sr^{2+} adsorption on the plain and hydrothermally modified (3 h reaction) TiO_2 and TiO_2/SiO_2 fibers at pH 11.5 were excellent, 338,000–3,490,000 mL g^{-1} (Fig. 12, Table 3). The hydrothermally modified TiO_2 and $3TiO_2$–$1SiO_2$ fibers performed better than the plain fibers. As regards the $1TiO_2$–$1SiO_2$ fibers, the K_d values for the plain and hydrothermally modified fibers were almost the same, 644,000 and 678,000 mL g^{-1}, respectively. The weaker Sr^{2+} uptake by the hydrothermally modified $1TiO_2$–$1SiO_2$ fibers compared with the hydrothermally modified $3TiO_2$–$1SiO_2$ and TiO_2 fibers is probably owing to the sparse growth and varying morphology of the TiO_2 nanorods on the $1TiO_2$–$1SiO_2$ fibers (Fig. 5f and g).

As can be seen from the standard deviation of ± 205,000 mL g^{-1} of the K_d value for the plain TiO_2 fibers, the Sr^{2+} uptake by the TiO_2 fibers varied greatly in different experiments. Therefore, a clear comparison of Sr^{2+} uptake by the plain fibers is difficult. However, the results imply that the uptake was slightly more effective by the $1TiO_2$–$1SiO_2$ fibers than by the TiO_2 and $3TiO_2$–$1SiO_2$ fibers. The good Sr^{2+} uptake by the $1TiO_2$–$1SiO_2$ fibers might be explained by that besides TiO_2, SiO_2 also

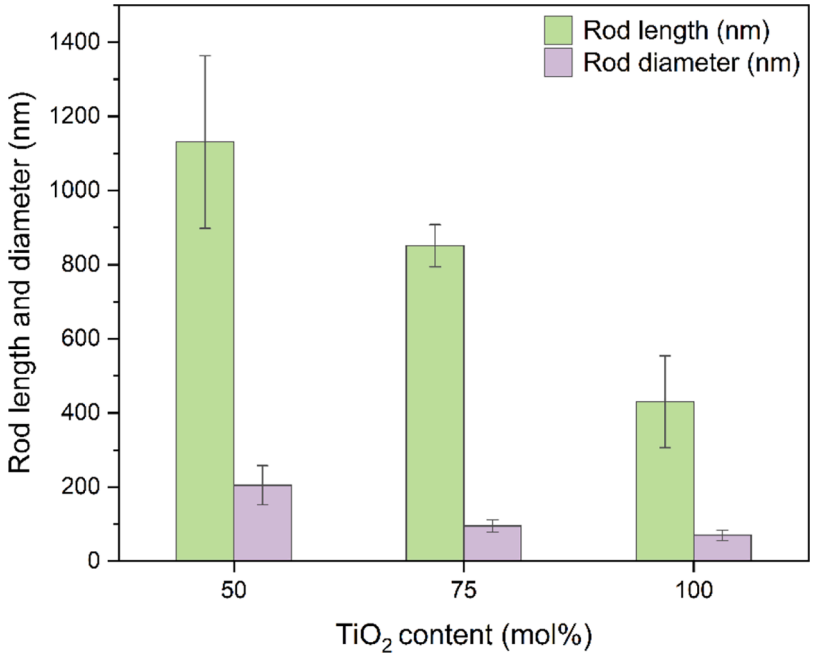

Fig. 7. Average length and diameter with standard deviation of hydrothermally grown (3 h reaction) TiO_2 nanorods on $1TiO_2$–$1SiO_2$, $3TiO_2$–$1SiO_2$ and TiO_2 fibers.

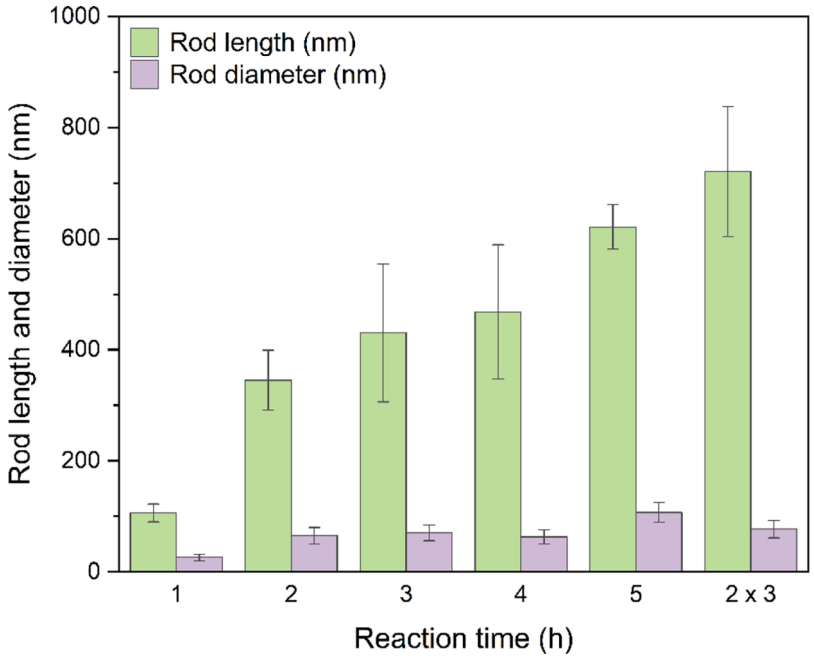

Fig. 8. Average length and diameter with standard deviation of hydrothermally grown TiO_2 nanorods on TiO_2 fibers as a function of reaction time.

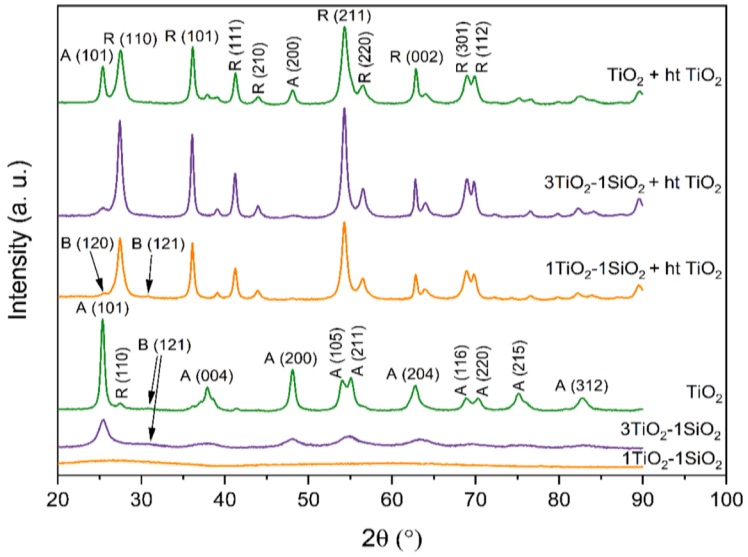

Fig. 9. X-ray diffraction patterns of plain and hydrothermally modified (ht TiO_2, 3 h reaction) TiO_2 and TiO_2/SiO_2 fibers. A, B and R denote anatase, brookite and rutile, respectively.

Table 2
Specific surface area, pore volume and average pore diameter of plain and hydrothermally modified (ht TiO_2, 3 h reaction) TiO_2 fibers.

Fibers	A_{BET} ($m^2\ g^{-1}$)	$V_{pore\ total}$ ($cm^3\ g^{-1}$)	D_{pore} (nm)
TiO_2	4.8	0.0080	6.4
TiO_2 + ht TiO_2	24	0.053	8.3

participates in the Sr^{2+} adsorption, since sorption of Sr^{2+} by amorphous SiO_2 is known [59]. Additionally, the amorphous SiO_2 component may improve the mechanical properties and durability of the fibers.

The superior performance of the hydrothermally modified TiO_2 and $3TiO_2$–$1SiO_2$ fibers compared with the plain fibers is evidently related to their larger surface area. The large surface area, in turn, stems from the thick nanorod coating and the polycrystallinity of both the substrate fibers and the nanorods. Moreover, both anatase and rutile TiO_2 are able to efficiently uptake Sr^{2+}, since the plain fibers consist predominantly of anatase (53–76 wt%, Table 1) and the hydrothermally modified fibers consist predominantly of rutile (83–97 wt%, Table 1). This is supported by previous studies on Sr^{2+} adsorption by anatase [7–9,13,14] and rutile [15,16] TiO_2 nanoparticles and rutile TiO_2 single crystals [15]. Sr^{2+} possibly adsorbs on the brookite surface too. EDX spectra and semi-quantitative elemental analysis results of the plain and hydrothermally modified TiO_2 fibers and the plain $3TiO_2$–$1SiO_2$ and $1TiO_2$–$1SiO_2$ fibers after adsorption of Sr^{2+} are shown in Fig. S8–S11.

3.5.3. *Effect of competing ions*

Selectivity towards a specific ion is essential for an effective adsorbent. This is especially important for nuclear wastewater treatment as there is usually only a trace concentration of the target radionuclide

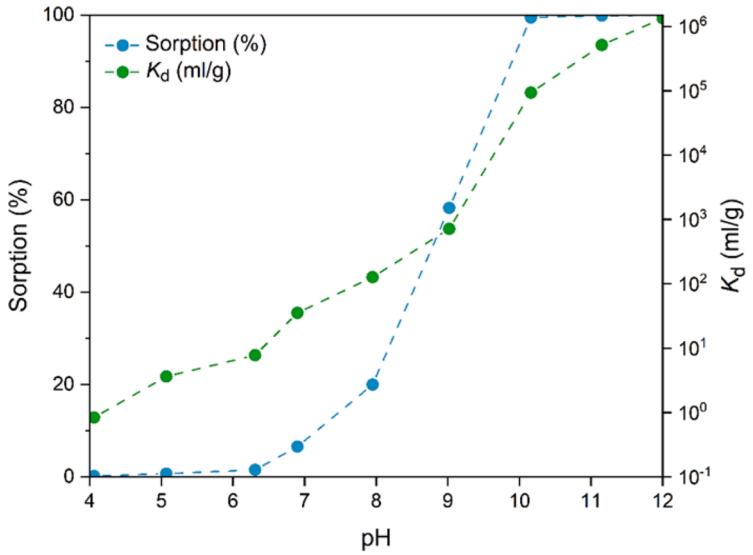

Fig. 10. Sorption and distribution coefficient (K_d) of $^{85}Sr^{2+}$ on TiO_2 fibers as a function of pH in 0.01 M $NaNO_3$ (2 g L^{-1} TiO_2, 30 Bq mL^{-1} $^{85}Sr^{2+}$).

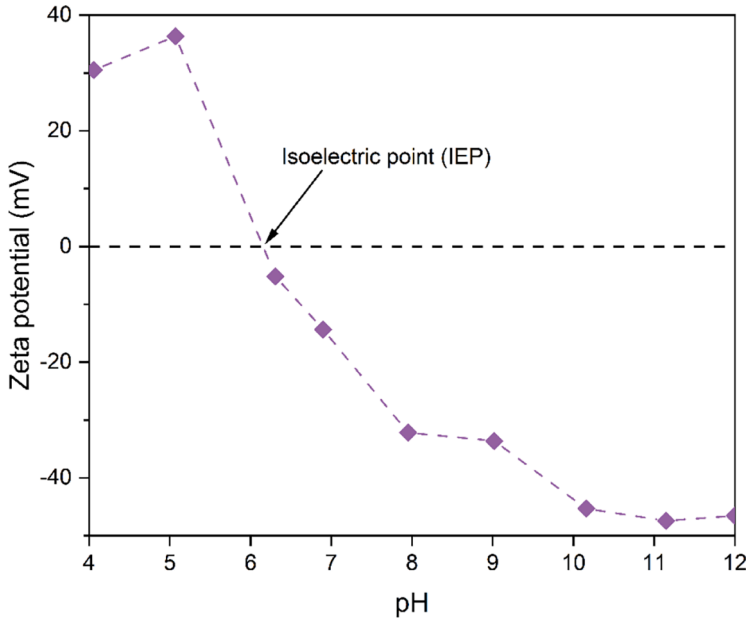

Fig. 11. Zeta potential of TiO_2 fibers as a function of pH after adsorption of $^{85}Sr^{2+}$ in 0.01 M $NaNO_3$ (2 g L^{-1} TiO_2, 30 Bq mL^{-1} $^{85}Sr^{2+}$).

among much larger concentrations of other ions. Na^+, Mg^{2+}, Ca^{2+} and trace amounts of Ba^{2+} exist in natural and in most nuclear wastewaters, and Na^+, Mg^{2+} and Ca^{2+} are the major competing ions in the radionuclide removal. As alkaline earth metals, Mg^{2+}, Ca^{2+} and Ba^{2+} also have similar chemical properties as Sr^{2+}. Therefore, the interfering influence of the four ions on the Sr^{2+} uptake by the TiO_2 fibers was studied at pH 9. Sr^{2+} sorption at the same Na^+ concentration as used in the pH effect experiment (Fig. 10), 0.01 M, was set as a reference value and the results were compared with it. Concentration of 0.01 M was used for Mg^{2+}, Ca^{2+} and Ba^{2+} and concentrations of 0.001, 0.01, 0.1 and 1 M were used for Na^+. $^{85}Sr^{2+}$ concentration was 30 Bq mL^{-1}. As shown in Fig. 13, Na^+ and Mg^{2+} interfered with the Sr^{2+} uptake only moderately while Ca^{2+} and Ba^{2+} interfered more. This is promising for the use of the fibers for nuclear wastewater purification because Na^+ and Mg^{2+} are more abundant (0.47 and 0.05 M in sea water, respectively) than Ca^{2+} and Ba^{2+} (0.01 M and 0.09 μM in sea water, respectively). In a nuclear waste effluent in the pH range of 10–12 where the Sr^{2+} uptake by the TiO_2 fibers is the best, Ca^{2+} and Ba^{2+} are not likely to interfere as much as in the laboratory experiment at pH 9 because of the lower water solubility of $Ca(OH)_2$ than that of $Sr(OH)_2$ and the small concentration of Ba^{2+}. Sodium nonatitanate ($Na_4Ti_9O_{20}{\cdot}nH_2O$) powder for instance has been reported to adsorb more Sr^{2+} than Ca^{2+} at pH 10 [60].

3.5.4. *Durability of the hydrothermally modified fibers in column operation*

In industrial wastewater treatment, a continuous column mode operation with packed sorbent beds is more effective than operation in a batch mode [61]. Hence, the durability of the hydrothermally modified TiO_2 fibers (3 h reaction) packed into a flow-through column was tested (Fig. S17). FESEM images of the fibers before packing into the column are shown in Fig. S18a–c. Fig. S18d–f show the fibers after packing but before solution flow and no damage caused by the packing of fibers can be seen. After the solution flow, only minor damage to the fibers such as detachment of individual nanorods was observed at flow rates up to 19 mL h^{-1} (Fig. S18g–i). This was confirmed by determining average

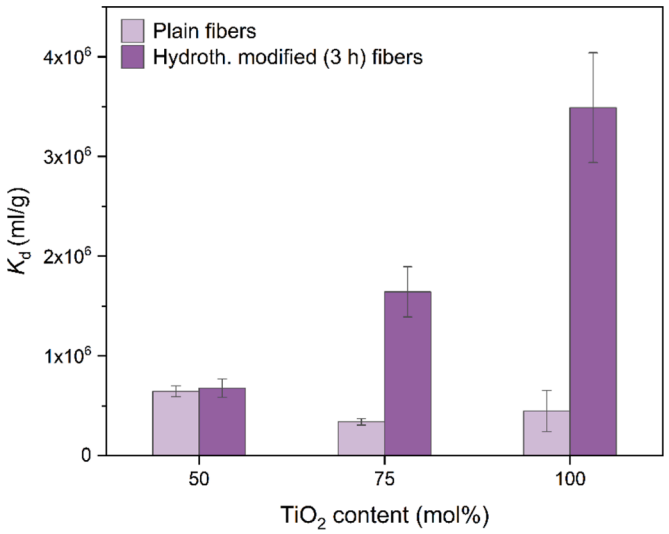

Fig. 12. Distribution coefficient (K_d) with standard deviation of $^{85}Sr^{2+}$ on plain and hydrothermally modified (3 h reaction) TiO_2, $3TiO_2$–$1SiO_2$ and $1TiO_2$–$1SiO_2$ fibers in 0.1 M $NaNO_3$ at pH 11.5 (2 g L^{-1} adsorbent, 100 Bq mL^{-1} $^{85}Sr^{2+}$).

Table 3
Sorption and distribution coefficient (K_d) of $^{85}Sr^{2+}$ on plain and hydrothermally modified (ht TiO_2, 3 h reaction) TiO_2 and TiO_2/SiO_2 fibers in 0.1 M $NaNO_3$ at pH 11.5 (2 g L^{-1} adsorbent, 100 Bq mL^{-1} $^{85}Sr^{2+}$).

Fibers	Sorption (%)	K_d (mL g^{-1})
$1TiO_2$–$1SiO_2$	99.89 ± 0.02	644,000 ± 54,000
$3TiO_2$–$1SiO_2$	99.85 ± 0.01	338,000 ± 16,000
TiO_2	99.86 ± 0.07	447,000 ± 205,000
$1TiO_2$–$1SiO_2$ + ht TiO_2	99.89 ± 0.02	678,000 ± 92,000
$3TiO_2$–$1SiO_2$ + ht TiO_2	99.97 ± 0.002	1,642,000 ± 252,000
TiO_2 + ht TiO_2	99.99 ± 0.002	3,490,000 ± 551,000

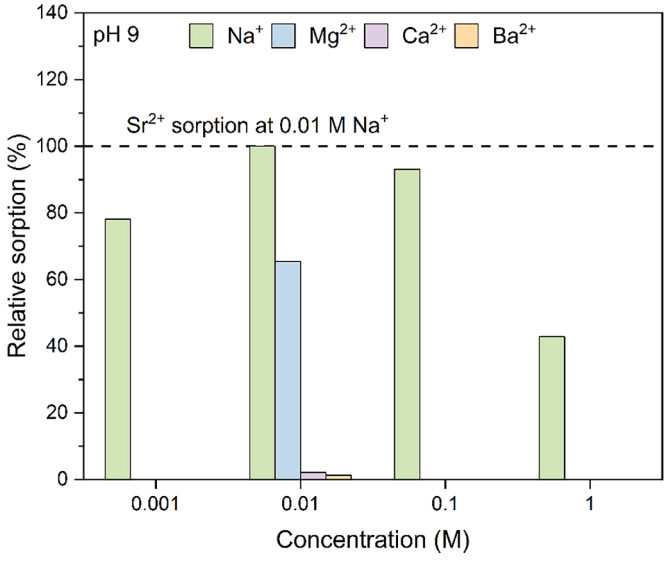

Fig. 13. Effect of 0.001–1 M Na^+ and 0.01 M Mg^{2+}, Ca^{2+} and Ba^{2+} on $^{85}Sr^{2+}$ sorption by TiO_2 fibers at pH 9 (4 g L^{-1} TiO_2 for Na^+, 2 g L^{-1} TiO_2 for Mg^{2+}, Ca^{2+} and Ba^{2+}, 30 Bq mL^{-1} $^{85}Sr^{2+}$). The dashed line shows the reference value at the same Na^+ concentration as used in the pH effect experiment (Fig. 10).

lengths and diameters of the nanorods before and after the test with a Fiji ImageJ software. For the flow rates 5–19 mL h^{-1} the nanorod average dimensions didn't change during the test. Slightly more extensive damage such as detachment of a larger number of nanorods was observed to the fibers that were exposed to flow rates of 37 and 74 mL h^{-1} (Fig. S18j–o). Image analysis also revealed that the nanorods had become on average somewhat shorter and thinner after being exposed to the higher flow rates which implies that there may have been some wear of the nanorods. The results are encouraging for the industrial use of the hydrothermally modified fibers since in the adsorption column operation, the optimum throughput performance is achieved by using flow rates as low as possible [61].

4. Conclusions

By a novel facile and efficient electroblowing technique, we have prepared high-quality submicron TiO_2 and composite TiO_2/SiO_2 fibers with Ti : Si molar ratios of 3 : 1 ($3TiO_2$–$1SiO_2$) and 1 : 1 ($1TiO_2$–$1SiO_2$). All the fibrous mats were durable and elastic, but the amorphous SiO_2 component improved the mechanical properties of the $1TiO_2$–$1SiO_2$ fibers. After calcination at 500 °C, the TiO_2 and $3TiO_2$–$1SiO_2$ fibers had a predominantly anatase structure with portions of brookite and rutile whereas the $1TiO_2$–$1SiO_2$ fibers were quasi-amorphous. The SiO_2 component hindered the crystal growth of the TiO_2/SiO_2 fibers. A layer of rutile TiO_2 nanorods was grown on the fibers by a hydrothermal method. The rods seemed to grow solely on the TiO_2 domains of the fiber surface which affected their size and morphology. In batch adsorption experiments, all the fibers showed excellent Sr^{2+} uptake and the hydrothermally modified fibers performed better than the plain fibers. The hydrothermally modified TiO_2 fibers had the highest K_d value of 3,490,000 mL g^{-1}. The superior Sr^{2+} uptake by the hydrothermally modified fibers is evidently based on their larger surface area owing to their morphology. The Sr^{2+} uptake results suggest that Sr^{2+} can adsorb on both anatase and rutile TiO_2. When exposed to dynamic flow-through column conditions, only slight wear was observed on the hydrothermally grown nanorods on the TiO_2 fibers which is promising for the use of the fibers in industrial scale column operation. The TiO_2 and TiO_2/SiO_2 submicron fibers with and without TiO_2 nanorod layers could be sustainable and cost-effective materials to remove ^{90}Sr from nuclear wastewaters.

Funding information

The research work was financially supported by Fortum Power and Heat Oy. The topic of the research was partly chosen in collaboration with the funder. Otherwise the funder was not involved in the conduct of the research nor in reporting the results in this article.

CRediT authorship contribution statement

Johanna Paajanen: Conceptualization, Methodology, Investigation, Data curation, Formal analysis, Validation, Visualization, Writing – original draft. **Lauri Pettilä:** Investigation, Data curation, Formal analysis. **Satu Lönnrot:** Investigation, Data curation, Formal analysis. **Mikko Heikkilä:** Formal analysis. **Timo Hatanpää:** Investigation, Formal analysis. **Mikko Ritala:** Funding acquisition, Supervision, Writing – review & editing. **Risto Koivula:** Funding acquisition, Supervision, Writing – review & editing.

Declaration of Competing Interest

The authors declare that they have no known competing financial interests or personal relationships that could have appeared to influence the work reported in this paper.

Data availability

Data will be made available on request.

Acknowledgements

Kaisu Ainassaari is thanked for conducting the BET and BJH analyses and Anton Vihervaara for providing the SiO_2 fibers. The use of ALD center Finland research infrastructure is acknowledged. Fortum Power and Heat Oy is gratefully acknowledged for financial support for the research.

Supplementary materials

Supplementary material associated with this article can be found, in the online version, at doi:10.1016/j.ceja.2022.100434.

References

[1] R. Koivula, R. Harjula, J. Lehto, Selective removal of radionuclides from nuclear waste effluents using inorganic ion exchangers, in: J.M. Loureiro, M.T. Kartel (Eds.), Combined and Hybrid Adsorbents, Nato Security Through Science Series C: Environmental Security, Springer, 2006, pp. 37–47.
[2] D. Alby, C. Charnay, M. Heran, B. Prelot, J. Zajac, Recent developments in nanostructured inorganic materials for sorption of cesium and strontium: synthesis and shaping, sorption capacity, mechanisms, and selectivity—a review, J. Hazard. Mater 344 (2018) 511–530, https://doi.org/10.1016/j.jhazmat.2017.10.047.
[3] United States Environmental Protection Agency (EPA), Radiation Protection, Radionuclide Basics: Strontium-90. https://www.epa.gov/radiation/radionuclide-basics-strontium-90 (accessed 15 July 2022).
[4] L.A. Malik, A. Bashir, A. Qureashi, A.H. Pandith, Detection and removal of heavy metal ions: a review, Environ. Chem. Lett. 17 (2019) 1495–1521, https://doi.org/10.1007/s10311-019-00891-z.
[5] S. Muthusaravanan, N. Sivarajasekar, J.S. Vivek, T. Paramasivan, Mu Naushad, J. Prakashmaran, V. Gayathri, O.K. Al-Duaij, Phytoremediation of heavy metals: mechanisms, methods and enhancements, Environ. Chem. Lett. 16 (2018) 1339–1359, https://doi.org/10.1007/s10311-018-0762-3.
[6] T.S. Anirudhan, F. Shainy, J.R. Deepa, Effective removal of Cobalt(II) ions from aqueous solutions and nuclear industry wastewater using sulfhydryl and carboxyl functionalised magnetite nanocellulose composite: batch adsorption studies, Chem. Ecol. 35 (2019) 235–255, https://doi.org/10.1080/02757540.2018.1532999.
[7] M.K. Ridley, M.L. Machesky, J.D. Kubicki, Experimental study of strontium adsorption on anatase nanoparticles as a function of size with a density functional theory and CD Model interpretation, Langmuir 31 (2015) 703–713, https://doi.org/10.1021/la503932e.
[8] S. Kasap, H. Tel, S. Piskin, Preparation of TiO_2 nanoparticles by sonochemical method, isotherm, thermodynamic and kinetic studies on the sorption of strontium, J. Radioanal. Nucl. Chem. 289 (2011) 489–495, https://doi.org/10.1007/s10967-011-1090-2.
[9] I. Mironyuk, I. Mykytyn, H. Vasylyeva, K. Savka, Sodium-modified mesoporous TiO_2: sol-gel synthesis, characterization and adsorption activity toward heavy metal cations, J. Mol. Liq. 316 (2020), 113840, https://doi.org/10.1016/j.molliq.2020.113840.
[10] K. Chen, C. Chen, X. Ren, A. Alsaedi, T. Hayat, Interaction mechanism between different facet TiO_2 and U(VI): experimental and density-functional theory investigation, Chem. Eng. J. 359 (2019) 944–954, https://doi.org/10.1016/j.cej.2018.11.092.
[11] G.A. Seisenbaeva, G. Daniel, V.G. Kessler, J.-.M. Nedelec, General facile approach to transition-metal oxides with highly uniform mesoporosity and their application as adsorbents for heavy-metal-ion sequestration, Chem. Eur. J. 20 (2014) 10732–10736, https://doi.org/10.1002/chem.201402691.
[12] D.E. Giammar, C.J. Maus, L. Xie, Effects of particle size and crystalline phase on lead adsorption to titanium dioxide nanoparticles, Environ. Eng. Sci. 24 (2007) 85–95, https://doi.org/10.1089/ees.2007.24.85.
[13] I. Mironyuk, T. Tatarchuk, H. Vasylyeva, M. Naushad, I. Mykytyn, Adsorption of Sr (II) cations onto phosphated mesoporous titanium dioxide: mechanism, isotherm and kinetics studies, J. Environ. Chem. Eng. 7 (2019), 103430, https://doi.org/10.1016/j.jece.2019.103430.
[14] I. Mironyuk, T. Tatarchuk, H. Vasylyeva, V.M. Gun'ko, I. Mykytyn, Effects of chemosorbed arsenate groups on the mesoporous titania morphology and enhanced adsorption properties towards Sr(II) cations, J. Mol. Liq. 282 (2019) 587–597, https://doi.org/10.1016/j.molliq.2019.03.026.
[15] A.van Veelen, P.C.M. Francisco, N.P. Edwards, J.F.W. Mosselmans, T. Sato, R. A. Wogelius, In situ EXAFS study of Sr adsorption on TiO_2(110) under high ionic strength wastewater conditions, Minerals (2021) 11, https://doi.org/10.3390/min11121386.
[16] M.K. Ridley, T. Hiemstra, W.H. van Riemsdijk, M.L. Machesky, Inner-sphere complexation of cations at the rutile–water interface: a concise surface structural interpretation with the CD and MUSIC model, Geochim. Cosmochim. Acta 73 (2009) 1841–1856, https://doi.org/10.1016/j.gca.2009.01.004.
[17] S. Lönnrot, V. Suorsa, J. Paajanen, T. Hatanpaa, M. Ritala, R. Koivula, Submicron fibers as a morphological improvement of amorphous zirconium oxide particles and their utilization in antimonate (Sb(v)) removal, RSC Adv. 9 (2019) 22355–22365, https://doi.org/10.1039/C9RA04211C.
[18] J. Paajanen, S. Weintraub, S. Lönnrot, M. Heikkilä, M. Vehkamäki, M. Kemell, T. Hatanpää, M. Ritala, R. Koivula, Novel electroblowing synthesis of tin dioxide and composite tin dioxide/silicon dioxide submicron fibers for cobalt(ii) uptake, RSC Adv. 11 (2021) 15245–15257, https://doi.org/10.1039/D1RA01559A.
[19] K.A. Gebru, C. Das, Removal of Pb (II) and Cu (II) ions from wastewater using composite electrospun cellulose acetate/titanium oxide (TiO_2) adsorbent, J. Water Process Eng. 16 (2017) 1–13, https://doi.org/10.1016/j.jwpe.2016.11.008.
[20] Ş. Parlayıcı, A. Yar, A. Avcı, E. Pehlivan, Removal of hexavalent chromium using polyacrylonitrile/titanium dioxide nanofiber membrane, Desalin. Water Treat. 57 (2016) 16177–16183, https://doi.org/10.1080/19443994.2015.1077349.
[21] S. Abbasizadeh, A.R. Keshtkar, M.A. Mousavian, Preparation of a novel electrospun polyvinyl alcohol/titanium oxide nanofiber adsorbent modified with mercapto groups for uranium(VI) and thorium(IV) removal from aqueous solution, Chem. Eng. J. 220 (2013) 161–171, https://doi.org/10.1016/j.cej.2013.01.029.
[22] J. Paajanen, S. Lönnrot, M. Heikkilä, K. Meinander, M. Kemell, T. Hatanpää, K. Ainassaari, M. Ritala, R. Koivula, Novel electroblowing synthesis of submicron zirconium dioxide fibers: effect of fiber structure on antimony(v) adsorption, Nanoscale Adv. 1 (2019) 4373–4383, https://doi.org/10.1039/C9NA00414A.
[23] W.S. Lee, Y.-.S. Park, Y.-.K. Cho, Significantly enhanced antibacterial activity of TiO_2 nanofibers with hierarchical nanostructures and controlled crystallinity, Analyst 140 (2015) 616–622, https://doi.org/10.1039/C4AN01682C.
[24] M. Ghosh, J. Liu, S.S.C. Chuang, S.C. Jana, Fabrication of hierarchical V_2O_5 nanorods on TiO_2 nanofibers and their enhanced photocatalytic activity under visible light, ChemCatChem 10 (2018) 3305–3318, https://doi.org/10.1002/cctc.201800172.
[25] S. Ramakrishna, K. Fujihara, W.-.E. Teo, T.-.C. Lim, Z. Ma, An Introduction to Electrospinning and Nanofibers, World Scientific, Singapore, 2005.
[26] S. Thenmozhi, N. Dharmaraj, K. Kadirvelu, H.Y. Kim, Electrospun nanofibers: new generation materials for advanced applications, Mater. Sci. Eng., B 217 (2017) 36–48, https://doi.org/10.1016/j.mseb.2017.01.001.
[27] Foshan Nanofiberlabs Co., Ltd. https://www.nanofiberlabs.com/(accessed 16 July 2022).
[28] Elmarco. https://www.elmarco.com/(accessed 16 July 2022).
[29] Inovenso Ltd. https://www.inovenso.com/(accessed 16 July 2022).
[30] Fanavaran Nano-Meghyas, FNM Co. Ltd, 16 July 2022. http://en.fnm.ir/(accessed.
[31] J.L. Daristotle, A.M. Behrens, A.D. Sandler, P. Kofinas, A review of the fundamental principles and applications of solution blow spinning, ACS Appl. Mater. Interfaces 8 (2016) 34951–34963, https://doi.org/10.1021/acsami.6b12994.
[32] Z. Huang, A. Kolbasov, Y. Yuan, M. Cheng, Y. Xu, R. Rojaee, R. Deivanayagam, T. Foroozan, Y. Liu, K. Amine, J. Lu, A.L. Yarin, R. Shahbazian-Yassar, Solution blowing synthesis of Li-conductive ceramic nanofibers, ACS Appl. Mater. Interfaces 12 (2020) 16200–16208, https://doi.org/10.1021/acsami.9b19851.
[33] W. Tutak, S. Sarkar, S. Lin-Gibson, T.M. Farooque, G. Jyotsnendu, D. Wang, J. Kohn, D. Bolikal, C.G. Simon Jr., The support of bone marrow stromal cell differentiation by airbrushed nanofiber scaffolds, Biomaterials 34 (2013) 2389–2398, https://doi.org/10.1016/j.biomaterials.2012.12.020.
[34] E.N. Bolbasov, K.S. Stankevich, E.A. Sudarev, V.M. Bouznik, V.L. Kudryavtseva, L. V. Antonova, V.G. Matveeva, Y.G. Anissimov, S.I. Tverdokhlebov, The investigation of the production method influence on the structure and properties of the ferroelectric nonwoven materials based on vinylidene fluoride - tetrafluoroethylene copolymer, Mater. Chem. Phys. 182 (2016) 338–346, https://doi.org/10.1016/j.matchemphys.2016.07.041.
[35] I. Um, D. Fang, B. Hsiao, A. Okamoto, B. Chu, Electro-spinning and electro-blowing of hyaluronic acid, Biomacromolecules 5 (2004) 1428–1436, https://doi.org/10.1021/bm034539b.
[36] H.-.Y. Hsiao, C.-.M. Huang, Y.-.Y. Liu, Y.-.C. Kuo, H. Chen, Effect of air blowing on the morphology and nanofiber properties of blowing-assisted electrospun polycarbonates, J. Appl. Polym. Sci. 124 (2012) 4904–4914, https://doi.org/10.1002/app.35599.
[37] J. Holopainen, M. Ritala, Rapid production of bioactive hydroxyapatite fibers via electroblowing, J. Eur. Ceram. Soc. 36 (2016) 3219–3224, https://doi.org/10.1016/j.jeurceramsoc.2016.05.011.
[38] W.-.T. Kim, D.-.C. Park, W.-.H. Yang, C.-.H. Cho, W.-.Y. Choi, Effects of electrospinning parameters on the microstructure of PVP/TiO_2 nanofibers, Nanomaterials 11 (2021), https://doi.org/10.3390/nano11061616.
[39] O.V. Otieno, E. Csáki, O. Kéri, L. Simon, I.E. Lukács, K.M. Szécsényi, I.M. Szilágyi, Synthesis of TiO_2 nanofibers by electrospinning using water-soluble Ti-precursor, J. Therm. Anal. Calorim. 139 (2020) 57–66, https://doi.org/10.1007/s10973-019-08398-z.
[40] J.Z. Soo, L.C. Chai, B.C. Ang, B.H. Ong, Enhancing the antibacterial performance of titanium dioxide nanofibers by coating with silver nanoparticles, ACS Appl. Nano Mater. 3 (2020) 5743–5751, https://doi.org/10.1021/acsanm.0c00925.
[41] P. Aghasiloo, M. Yousefzadeh, M. Latifi, R. Jose, Highly porous TiO_2 nanofibers by humid-electrospinning with enhanced photocatalytic properties, J. Alloys Compd. 790 (2019) 257–265, https://doi.org/10.1016/j.jallcom.2019.03.175.
[42] V.N. Nguyen, M.T. Doan, M.V. Nguyen, Photoelectrochemical water splitting properties of CdS/TiO_2 nanofibers-based photoanode, J. Mater. Sci.: Mater. Electron. 30 (2019) 926–932, https://doi.org/10.1007/s10854-018-0363-8.

[43] B.S. Chapman, S.R. Mishra, J.B. Tracy, Direct Electrospinning of Titania Nanofibers with Ethanol, 48, Dalton Trans, 2019, pp. 12822–12827, https://doi.org/10.1039/C9DT01872G.
[44] O. Kéri, P. Bárdos, S. Boyadjiev, T. Igricz, Z.K. Nagy, I.M. Szilágyi, Thermal properties of electrospun polyvinylpyrrolidone/titanium tetraisopropoxide composite nanofibers, J. Therm. Anal. Calorim. 137 (2019) 1249–1254, https://doi.org/10.1007/s10973-019-08030-0.
[45] F. Huang, B. Motealleh, W. Zheng, M.T. Janish, C.B. Carter, C.J. Cornelius, Electrospinning amorphous SiO_2-TiO_2 and TiO_2 nanofibers using sol-gel chemistry and its thermal conversion into anatase and rutile, Ceram. Int. 44 (2018) 4577–4585, https://doi.org/10.1016/j.ceramint.2017.10.134.
[46] J. Wang, X. An, Y. Yu, X. Li, M. Ge, Er-doped titanium dioxide/silicon dioxide fibres with enhanced photodegradation performance, Micro Nano Lett 13 (2018) 297–301, https://doi.org/10.1049/mnl.2017.0541.
[47] D.L. Costa, R.S. Leite, G.A. Neves, L.N. de L. Santana, E.S. Medeiros, R.R. Menezes, Synthesis of TiO_2 and ZnO nano and submicrometric fibers by solution blow spinning, Mater. Lett. 183 (2016) 109–113, https://doi.org/10.1016/j.matlet.2016.07.073.
[48] L. Lutterotti, D. Chateigner, S. Ferrari, J. Ricote, Texture, residual stress and structural analysis of thin films using a combined X-ray analysis, Thin Solid Films 450 (2004) 34–41, https://doi.org/10.1016/j.tsf.2003.10.150.
[49] C. Peniche, D. Zaldivar, M. Pazos, S. Paz, A. Bulay, J. Roman, Study of the thermal degradation of poly(N-vinyl-2-pyrrolidone) by thermogravimetry-FTIR, J. Appl. Polym. Sci. 50 (1993) 485–493, https://doi.org/10.1002/app.1993.070500312.
[50] H.A. Khizir, T.A.-H. Abbas, Hydrothermal synthesis of TiO_2 nanorods as sensing membrane for extended-gate field-effect transistor (EGFET) pH sensing applications, Sens. Actuators, A 333 (2022), 113231, https://doi.org/10.1016/j.sna.2021.113231.
[51] B. Arjunkumar, G. Ramalingam, M. Ramesh, J.S. Ponraj, K.V. Rao, Investigation of uni-directional nanorods composed microspheres and branched TiO_2 nanorods towards solar cell application, Mater. Lett. 273 (2020), 127900, https://doi.org/10.1016/j.matlet.2020.127900.
[52] A. Prathan, J. Sanglao, T. Wang, C. Bhoomanee, P. Ruankham, A. Gardchareon, D. Wongratanaphisan, Controlled structure and growth mechanism behind hydrothermal growth of TiO_2 nanorods, Sci. Rep. 10 (2020) 8065, https://doi.org/10.1038/s41598-020-64510-6.
[53] S. Issar, A.K. Mahapatro, Hydrothermally grown rutile titanium dioxide nanostructures with various morphologies, Mater. Sci. Semicond. Process. 104 (2019), 104676, https://doi.org/10.1016/j.mssp.2019.104676.
[54] S.M. Mokhtar, M.K. Ahmad, C.F. Soon, N. Nafarizal, A.B. Faridah, A.B. Suriani, M. H. Mamat, M. Shimomura, K. Murakami, Fabrication and characterization of rutile-phased titanium dioxide (TiO_2) nanorods array with various reaction times using one step hydrothermal method, Optik (Stuttg) 154 (2018) 510–515, https://doi.org/10.1016/j.ijleo.2017.10.091.
[55] S.S. Mali, H. Kim, C.S. Shim, P.S. Patil, J.H. Kim, C.K. Hong, Surfactant free most probable TiO_2 nanostructures via hydrothermal and its dye sensitized solar cell properties, Sci. Rep. 3 (2013) 3004, https://doi.org/10.1038/srep03004.
[56] Y. Wang, H. Huang, J. Gao, G. Lu, Y. Zhao, Y. Xu, L. Jiang, TiO_2-SiO_2 composite fibers with tunable interconnected porous hierarchy fabricated by single-spinneret electrospinning toward enhanced photocatalytic activity, J. Mater. Chem. A 2 (2014) 12442–12448, https://doi.org/10.1039/c4ta01208a.
[57] S. Murugesan, R. Thirumurugesan, E. Mohandas, P. Parameswaran, X-ray diffraction Rietveld analysis and Bond Valence analysis of nano titania containing oxygen vacancies synthesized via sol-gel route, Mater. Chem. Phys. 225 (2019) 320–330, https://doi.org/10.1016/j.matchemphys.2018.12.061.
[58] N.L. Hakem, I. Al Mahamid, J.A. Apps, G.J. Moridis, Sorption of cesium and strontium on Hanford soil, J. Radioanal. Nucl. Chem. 246 (2000) 275–278, https://doi.org/10.1023/A:1006701902891.
[59] S.A. Carroll, S.K. Roberts, L.J. Criscenti, P.A. O'Day, Surface complexation model for strontium sorption to amorphous silica and goethite, Geochem. Trans. 9 (2008) 2, https://doi.org/10.1186/1467-4866-9-2.
[60] A. Villard, G. Toquer, B. Siboulet, P. Trens, A. Grandjean, J.-F. Dufrêche, Sorption pH dependance of strontium/calcium by sodium nonatitanate, Chemosphere 202 (2018) 33–39, https://doi.org/10.1016/j.chemosphere.2018.02.017.
[61] J. Lehto, R. Koivula, H. Leinonen, E. Tusa, R. Harjula, Removal of radionuclides from Fukushima Daiichi waste effluents, Sep, Purif. Rev. 48 (2019) 122–142, https://doi.org/10.1080/15422119.2018.1549567.